https://dx.doi.org/10.1016/j.ijbiomac.2023.127000

A Sandwich-Like Silk Fibroin/Polysaccharide Composite Dressing with continual biofluid draining for wound exudate management

Yixin Wang,[a,b] Haoyu Wang,[a,b] Bitao Lu,[a,b] Kun Yu,[a,b] Ruiqi Xie,[a,b] Guangqian Lan,[a,b]
Jing Xie,[c,*] Enling Hu, [a,d,*] Fei Lu [a,b,*]

[a] State Key Laboratory of Resource Insects, College of Sericulture, Textile and Biomass Sciences, Southwest University, Chongqing 400715, China

[b] Chongqing Engineering Research Center of Biomaterial Fiber and Modern Textile, Chongqing 400715, China

[c] Department of Stomatology, The First Affiliated Hospital of Wenzhou Medical University, Wenzhou 325000, China

[d] School of Fashion and Textiles, The Hong Kong Polytechnic University, Kowloon, Hong Kong

Abstract: Optimal wound healing requires a wet microenvironment without over-hydration. Inspired by capillarity and transpiration, we have developed a sandwich-like fibers/sponge dressing with continuous exudate drainage to maintain appropriate wound moisture. This dressing is prepared by integrating a three-layer structure using the freeze-drying method. Layer I, as the side that contacts with the skin directly, consists of a hydrophobic silk fibroin membrane; Layer II, providing the pumping action, is made of superabsorbent chitosan-konjac glucomannan sponge; Layer III, accelerating evaporation sixfold compared to natural evaporation, is constructed with a

---

[*] Corresponding author. E-mail address: lufei2111217@iccas.ac.cn (Fei Lu); enling.allen.hu@connect.polyu.hk (Enling Hu); xiejing@wmu.edu.cn (Jing Xie).

graphene oxide soaked hydrophilic cellulose acetate membrane. Animal experiments showed that the composite dressing had superior wound-healing characteristics, with wounds decreasing to 24.8% of their original size compared to 28.5% for the commercial dressing and 43.2% for the control. The enhanced wound healing can be ascribed to the hierarchical porous structure serves as the fluid-driving factor in this effort; the hydrophilicity of a membrane composed of silk fibroin nanofibers is adjustable to regulate fluid-transporting capacity; and the photothermal effect of graphene oxide guarantees exudates that have migrated to the top layer to evaporate continuously. These findings indicate the unidirectional wicking dressing has the potential to become the next generation of clinical dressings.

Keywords: Unidirectional Wicking; Photothermal Effect; Wound Healing.

1. Introduction

Healthcare has always been a critical issue closely related to people's lives, particularly in wound healing.[1, 2] Wound dressings play a pivotal role in safeguarding the wound bed, providing a suitable microenvironment to promote wound healing.[3] The optimum management of wound exudate in the microenvironment of the wound is crucial to tissue repair. A large volume of exudate can ultimately interfere with cell proliferation and hinder the healing process, as exudates may adversely provide an environment for bacterial and pathogen growth. [4] Although traditional moisture-absorbing dressings, such as gauzes[5], biocompatible hydrogels[6], and porous sponges[7], can initially absorb a certain amount of exudate to create a relatively low-water-content microenvironment for the wound, excess exudate will eventually accumulate over the wound interface, leading to over-hydration of the surrounding wound tissues, which inhibits the wound healing process.[8, 9] Therefore, there is an urgent need to design versatile new dressings capable of removing excessive biofluid dynamically while maintaining a suitable moist microenvironment for the wound without over-hydration.

Recently, several biomaterials have been developed with directional water transport capabilities to control the biofluids from wounds.[10] Based on the different mechanisms of unidirectional water transport, these materials can be generally classified into three categories. The first is the differential capillary effect. Researchers constructed multi-scaled interconnected dual-layer porous membranes with remarkable directional moisture transport using narrow diameter high-performance polyacrylonitrile nanofibers at the bottom and larger polyurethane (PU) fibers at the top.[11] The second category is the wetting gradient effect. Ding et al. fabricated wetting gradient composite membranes by combining a hydrophobic layer of polyethylene terephthalate nonwovens with a hydrophilic layer of polyamide.[12] The third category is inspired by plant transpiration.[13] According to this mechanism, Wang et al. emulated the antigravity directional water transport and ultrafast evaporation of natural Murray networks, which played important roles in the transpiration process of vascular plants.[14] Given that the treatment of traumatic exudate is highly dependent on the wettability of the dressing’s surface,[15] a hydrophilic-hydrophobic asymmetric structure based on the wetting gradient effect tends to be favored over these conventional methods due to its ease and effectiveness.[16, 17]

Constructing a typical membrane for unidirectional moisture transport requires a Janus structure with at least two heterogeneous layers with opposite hydrophilic and hydrophobic properties. Typically, the inner membrane that contacts the skin should be hydrophobic, while the outer membrane that is exposed to air should be hydrophilic. The Janus materials enable the creation of a surface wettability gradient, which allows for directional water transport and prevents backflow.[18, 19] For example, Shi et al. prepared a self-pumping dressing by electrospinning hydrophobic PU nanofiber membrane onto the hydrophilic medical gauze.[20] Zhang et al. utilized hydrophobic nanoparticles sprayed onto the surface of the oxygen plasma-treated PU sponges to produce a Janus dressing for wound management.[8] Hu et al. designed a bilayer nanoPE membrane with asymmetric microtopology and anisotropic wettability, which rapidly drained sweat and enhances physiological comfort.[21] By reviewing of these attempts, although Janus materials with surface wettability gradient could fairly transport wound exudate, most of these materials were made of complicated-to-prepare synthetic polymers, such as PU, which goes against the concept of sustainable development.[22] In addition, continuity in the management of exudates has not yet been addressed.

Thus, this study presents a novel strategy to create a sandwich-like fibers/sponge dressing. The composite dressing features a hierarchical porous three-layer structure: the superabsorbent chitosan-konjac glucomannan (CS/KGM) sponge (layer II) interlines into hydrophobic silk fibroin (SF) (layer I) and graphene oxide (GO)-soaked hydrophilic cellulose acetate (CA) membranes (layer III), as demonstrated in Figure 1. Sustainability, minimal cytotoxicity, and the ability to effectively manage exudate and regulate wound humidity make the composite dressing a promising new generation of wound dressings for clinical use.

2. Experimental Section

2.1. Materials

Silkworm cocoon (The State Key Laboratory of Silkworm Genome Biology, Southwest University, Chongqing, China). Cellulose acetate (Acetyl group: 39.8 wt%, hydroxyl: 3.5%, Shanghai Aladdin Biochemical Technology Co. Ltd, China). Graphene oxide monolayer dispersion (Chip diameter: 0.05-3 μm, Scientific compass, China).

Dialdehyde starch (Taian Jinshan Modified Starch Co. Ltd, China). Konjac glucomannan (Purity≥98%, Hefei Bomei Biotechnology Co. Ltd). Chitosan (Degree of deacetylation≥95%, viscosity: 100-200 mpa.s, Shanghai Macklin Biochemical Co. Ltd, China). The commercial dressing was purchased from Convid Medical Supplies Co. Ltd, China. CH_3COOH, NaOH, LiBr, and other unlisted reagents were commercially available.

2.2. Preparation of SF nanofiber membrane

Silk fibroin was extracted from Bombyx mori cocoons using a modified version of the previously described protocol.[23] In brief, the cocoons were degummed using $NaHCO_3$ solution (0.023 M) for 60 min at 100 °C and then washed with deionized water. Subsequently, the wholly dried SF fibers were solubilized in LiBr solution (9.3 M) at 60 °C for 4 h, followed by a dialysis process for 3 days. Finally, regenerated silk fibroin was centrifuged at 8000 rpm for 20 min and freeze-dried to obtain the SF sponge.

A 3wt% SF sponge was dissolved in hexafluoro-isopropanol with magnetic stirring for 4 hours at room temperature to prepare the electrospinning solution.[24] The as-prepared SF solution was transferred to a syringe (10 mL) with needles of 0.61 mm inner diameter, impelled at a rate of 0.6 mL/h. During the electrospinning process, a voltage of 20 kV was supplied on the spinneret, and the distance from the needle tip to the collector was 20 cm. The electrospinning time was set as 8 h. The SF nanofiber membranes were deposited on aluminized paper from the grounded drum collector.

The SF nanofiber membranes followed post-treatment by being submerged in ethanol for 1 and 7 hours at room temperature. Subsequently, these membranes were put in the fume hood to evaporate residual alcohol for further applications.

2.3. Preparation of CA nanofiber membrane

2.25 g of CA were thoroughly dissolved in 15 mL of acetone/DMF (2:1) by stirring for an hour at room temperature. The CA solution was injected into a syringe (10 mL) using a 0.52 mm metal needle. The syringe pump was used to squeeze out the polymer solution at a rate of 0.2 mL/h while the voltage was set at 16 kV, the needle tip was 15 cm from the collector, and the voltage was applied. The electrospinning time was set as 12 h. The aluminized paper was also utilized to collect the nanofiber membranes.

2.4. Preparation of the SF/CS-KGM Sponge/CA@GO (SSCG)

Based on our earlier report, the konjac glucomannan-chitosan solution was prepared to begin this process.[25] After post-treatment, the regenerated SF fiber membrane was spread on the bottom of the container ($4.5 \times 4.5\ cm^2$), and 10 mL of the konjac glucomannan-chitosan solution was poured on top of the SF membrane. To obtain 0.4, 1.2, and 2 mg/ml GO solutions, the graphene oxide dispersion was diluted with deionized water and uniformly shaken by ultrasonic. Finally, the CA nanofiber membrane was immersed in the three solutions mentioned above and exposed to a 3-minute ultrasonic shock before being placed on top of the konjac glucomannan-chitosan solution. The entire sample was subjected to vacuumization for 10 min to facilitate the penetration of the CS-KGM solution into the membranes. Subsequently, freeze-drying was carried out for 48 h to obtain SF/CS-KGM Sponge/CA@GO, designated as SSCG-1, SSCG-2, and SSCG-3, respectively.

2.5. Surface topography and structural characterization

Scanning electron microscopy (SEM, S-4800; Hitachi, Tokyo, Japan), water contact angle analyzer (JY-82B Kruss DSA, Germany), Fourier transform infrared spectrometer (FTIR, Bruker Vertex 70, Germany), Raman spectrum (532 nm, LabRam HR Evolution) and X-ray Diffraction Pattern (X-Pert-PRO; PANalytical) were adopted to characterize the nanofiber membrane and composite dressing.

The composite dressing was cut into strips and immersed in water with stirring for 4 min. The stability of different layers was observed and photographed.

2.6. Light-heat characterization

The photothermal performance of the composite dressing was tested upon exposure to a NIR 808 nm laser (0.5 W/cm^2) at a distance of 15 cm for 60 s. Real-time thermal images and temperature variations at various composite material layers were captured using an infrared thermal imaging device. Here, the biofluids in the wound were simulated using PBS. The evaporation rate of samples under NIR light and natural conditions for 1 and 5 min was calculated.

2.7. Characterization of wet transport

The wet transport behavior of composites dressing with different post-processing times of SF membrane was tested. Optical images of the porous membranes and the water transport process through the nanofiber membrane were recorded by a digital video camera. 1 mL of red ink was added to both the SF and CA membrane sides for the convenience of observation.

2.8. Cytotoxicity assay

For this study, the SSCG samples (1.5×1.5×0.3 cm) were incubated with L929 cells for 24 h, as detailed in our previous research.[26] The cytocompatibility was estimated by the MTT assay and Live/Dead cell staining. Repeat 3 times for each sample.

2.9. *In vivo* wound healing studies and histological examination

Three circular wounds of 20 mm diameter with full excisional trauma were created on the dorsal skin of New Zealand rabbits (~ 2 kg). One wound was then uncovered as a control, and both the commercial dressing and the SSCG dressing were applied to the remaining wounds immediately. During the first three days, the SSCG-treated groups were exposed to NIR light for 5 minutes daily. The images of wound sites were observed on days 3, 9, and 15. Then, the relative wound area change was quantitated.

To evaluate the quality of wound healing, the corresponding wound tissue was excised and processed per the previous report after standardization.[27] Specifically, the tissue slices were treated by hematoxylin-eosin (H&E) staining for morphological evaluation and by Masson trichrome staining for collagen deposition analysis. Each section was observed using an optical microscope (X73, Olympus). Epidermal thickness was measured in 3 independent locations using ImageJ in H&E sections. Collagen density (as %) was determined through Masson trichrome staining images by calculating the ratio of blue-stained area to total area using Image J.

All animal experiments were approved by the Animal Ethics Committee and performed following the protocols approved by the National Teaching Center of Animal Science and Experiment, Southwest University, China (accreditation number of the investigator: SWU_LAC-20210625).

3. Results and Discussion

3.1. Design and characterization of SSCG

In this study, the sandwich-like fibers/sponge dressings with controllable water transport were designed based on three criteria: (A) the dressings can achieve an antigravity directional water transport; (B) the dressings must allow for rapid water transport based on the hydrophilic and hydrophobic gradient, and (C) the dressings must enable ultrafast water evaporation.

Criteria A could be satisfied by combining layers I & II (SF membranes with smaller pores and CS-KGM membranes with larger pores) to establish the hierarchical porous structure and anisotropic surface wettability. Since electrospinning offers the electrospun products with high specific surface area, deformable porous structure, and highly interconnected nanofibrous features, the electrospun SF membrane was selected as layer I of the composite dressing to provide a smaller porous structure, which could potentially simulate the framework structure of the extracellular matrix and provides an ideal biomimetic environment for wound care. In addition, the CS/KGM sponge with stable mechanical performance was set as layer II, providing a larger porous structure for highly absorbent and water-retaining abilities.

Criteria B could be realized by the combination of layers I & II (SF membranes with hydrophobicity and CS-KGM membranes with hydrophilicity) as well. Considering that the inherent hydrophilicity of SF may hinder water transportation, the electrospun SF membrane was post-processed with ethanol to reduce its surface wettability. The interaction of layers I & II could establish a hydrophobic-hydrophilic asymmetric structure, which results in a sufficient drainage force to transport bio-liquids from the hydrophobic SF membrane (layer I) to the hydrophilic CS/KGM sponge (layer II).

Criteria C could be fulfilled by the introduction of a GO-soaked CA membrane as layer III, which could evaporate bio-liquids continuously by the photothermal effect of GO to avoid over-hydration of wounds. As water absorption by the sponge alone would be saturated, hindering continuous exudate removal, the NIR light irradiation could trigger the strong photothermal effect of GO to increase the temperature of Lay III to accelerate exudate removal by evaporation.

When the composite dressing was applied over a wound with bio-liquids, hydrophobic layer I (with smaller pores) pushed bio-liquids away from wounds to hydrophilic layer II (with larger pores) first; then, layer II adsorbed and pumped bio-liquids to hydrophilic layer III; eventually, layer III released the bio-liquids into the external environment by evaporation for the photothermal effect of GO, to avoid over-hydration of the wound.

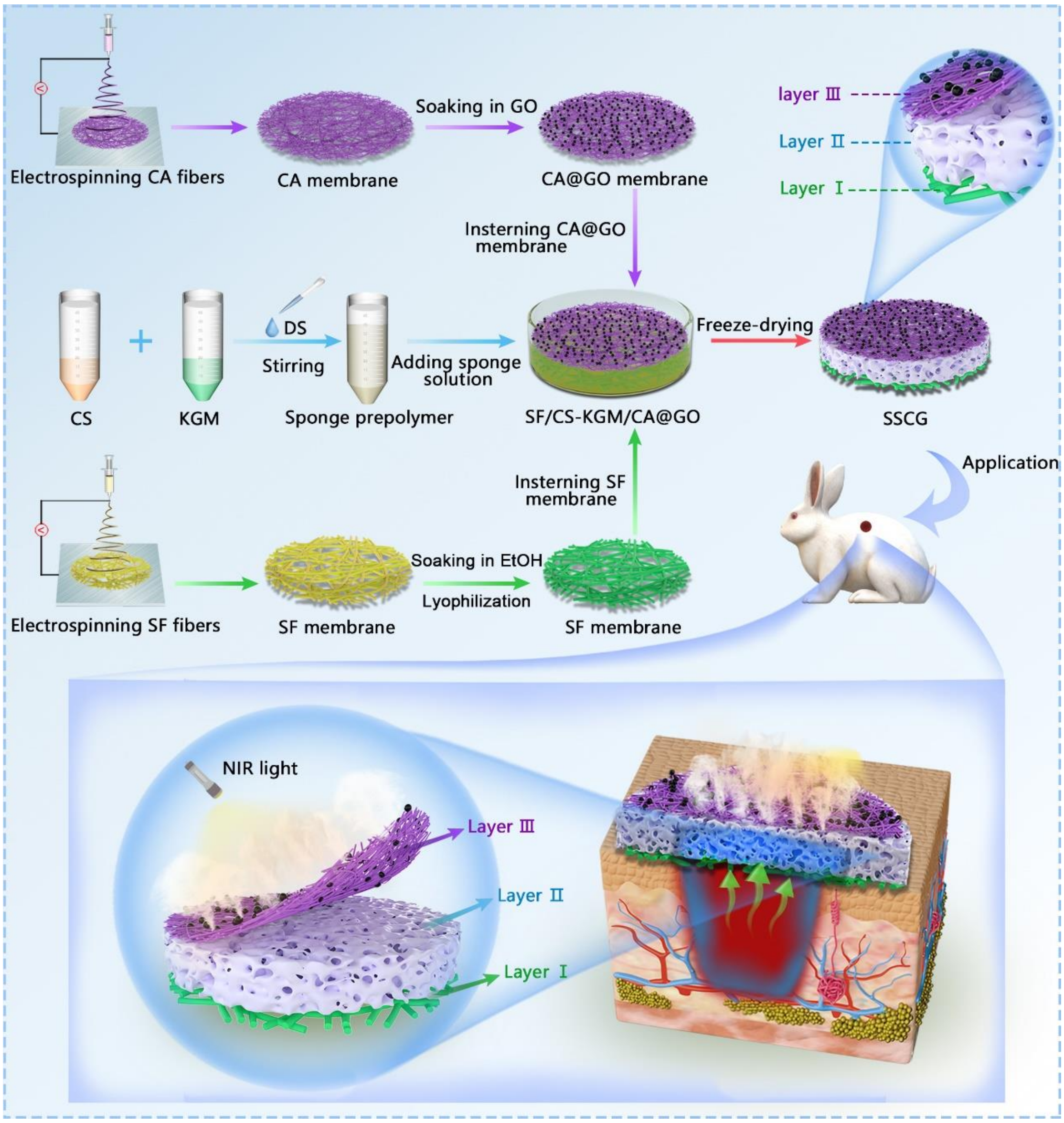

Figure 1. Schematic preparation of SSCG composite dressing and its exudate removal mechanism.

The SSCG composite dressing primarily consists of three layers, as shown in Figure 1. In order to construct a membrane-sponge-membrane sandwich-like structure, the SF and CA membranes were first prepared using electrospinning technology. The dissolvable SF membrane was treated with ethanol as layer I, and the CA membrane was doped with graphene oxide as layer III.

The SEM images demonstrate that both the initial and treated SF fibers were randomly oriented, as shown in Figure 2A. Additionally, the ethanol post-treatment conserved the SF membrane's numerous interconnected porous structures, which is advantageous for the transportation of water. The CA fibers served as layer III and had a thinner average diameter of ~ 425 nm than the SF fibers (~1.67 um). Furthermore, the image also exhibited the flake-like GO successfully attached to CA fibers. By contrast, the layer II of the superabsorbent sponge possesses a larger pore size (~385 μm). The pore size difference and surface wettability between the modified SF membrane and hydrophilic sponge endow them with the differential capillary effect, which is expected to improve the water-transport capacity. The cross-section morphology of the SSCG exhibited that both the SF and CA layer was tightly combined with the CS-KGM sponge, which would decrease the water-transport resistance at the interface of the membranes. The resulting unique hierarchical porous structure is crucial for achieving wet guidance. When the hydrophobic SF side was applied to the wound surface, tissue exudates got through the SF layer to be absorbed and stockpiled in the CS-KGM sponge. The high porosity provides a vital ability for moisture absorption for the composite dressing.

The stability of the sandwich-like composite is essential for the practical application. Thus, the bonding stability between layer II and other layers was tested. As detailed in Figure S1, it can be observed that the CS-KGM sponge quickly swells into a gel upon water absorption. Interestingly, both the SF membrane and the GO-soaked CA membrane exhibited strong adhesion to layer II even under water agitation. This can be attributed to the physical entanglement between the fibers and the sponge at the interfacial region.

As the SF layer is in direct contact with the wound, the hydrophobic property is essential to ensure it does not easily overhydrate wounds. Anhydrous ethanol treatment was chosen to weaken the hydrophilicity of the SF membrane. The water contact angles obviously change from 68° to 129° with increasing treatment time, which indicates that the SF membrane realizes the transformation from apparent hydrophilicity to hydrophobic behavior. This transformation is possibly associated with the changes of the crystalline structure and secondary structure of the silk protein. Herein, FTIR, Raman, and XRD spectroscopy were used to investigate it.

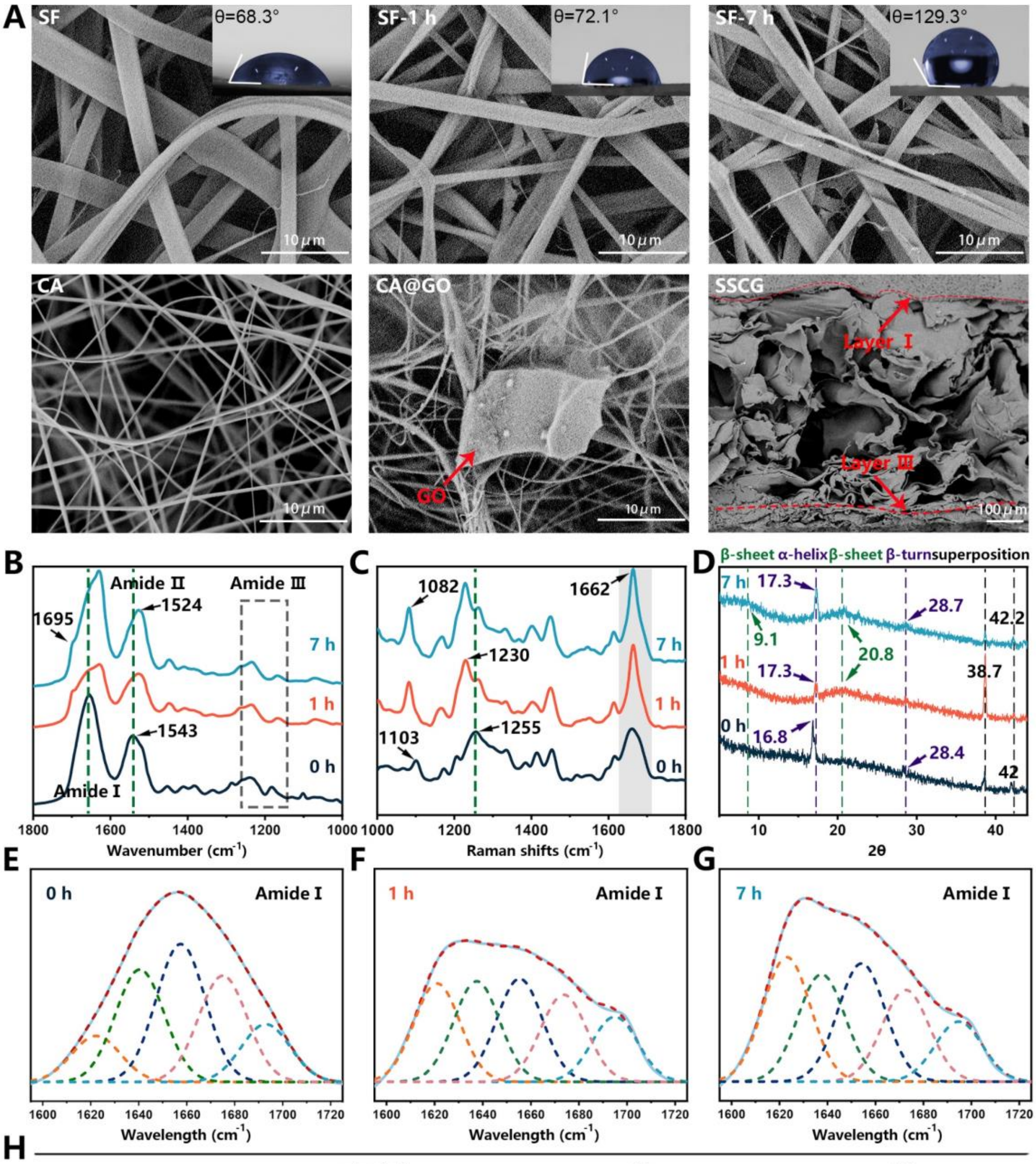

H

Secondary structure fractions	untreated		1 h		7 h	
	Peak position [cm^{-1}]	Area [%]	Peak position [cm^{-1}]	Area [%]	Peak position [cm^{-1}]	Area [%]
α-helix	1657	29.97	1655	22.72	1654	21.58
β-sheet	1622	9.97	1621	21.60	1623	24.78
β-turn	1675	23.08	1673	19.20	1672	18.29
Random coil	1640	24.43	1637	22.17	1637	21.39
Indetermination	1693	12.55	1694	14.31	1694	13.96

Figure 2. (A) SEM images of the initial SF membrane, post-processed SF membrane, CA membrane, CA membrane loaded with GO, and the cross-section of composite SSCG. (B-D) FTIR, Raman, and X-ray diffraction spectrum for initial and treated SF

analysis. (E-G) Deconvolution results of amide I band. (H) Variation of secondary structures content in silk protein after ethanol treatment.

3.2. The transformation of silk fibroin conformation

In Figure 2B, both the spectra of the initial and treated SF membranes were shown within the band region of 1800-1000 cm^{-1}. The standard amide bands, such as amide I (1720-1580 cm^{-1}), amide II (1580-1475 cm^{-1}), and amide III (1273-1142 cm^{-1}), are reserved for all samples.[28] However, following ethanol post-treatment, a noticeable redshift was observed in the amide I/II/III bands of the SF. Specifically, in comparison to the initial SF sample, the amide II peak of the treated sample (7h) shifted from 1543 cm^{-1} to 1524 cm^{-1} compared to the initial sample, suggesting the transition of the random coil to the β-sheet structure of the SF.[29] Additionally, the shoulder peak at 1695 cm^{-1} for the treated SF is related to the antiparallel arrangement of the fibroin chains in the β-sheet domains, demonstrating that the ethanol treatment caused a conformation transition of the silk fibroin.[30] To further evaluate the above influence of ethanol on the SF, the conducting deconvolution strategy was used to divide the amide I region into five peaks.[31] As shown in Figure 2 E-H, the amide I could be deconvoluted into five Gaussian peaks. The β-sheet as the main influencing factor of crystallinity was observed at around 1622 cm^{-1}. Alternatively, the rest structural contents α-helix, β-turn, and random roil were displayed at around 1657 cm^{-1}, 1675 cm^{-1}, and 1640 cm^{-1}, respectively. The content of the β-sheet increased dramatically as the treatment time increased, while the α-helix, β-turn and random roil all decreased at the same time (Figure S2), suggesting that the α-helix, β-turn, and random coil structure may transform into a β-sheet structure after treatment [32].

Raman spectrum was also used to evaluate the secondary structure of the SF membrane (Figure 2C). Specifically, both the initial and treated SF samples appeared the characteristic peak of the β-sheet structure located at 1662 cm^{-1} in the amide I region. However, the characteristic peaks of the post-treated samples were narrower and significantly more intense than those of the initial SF samples, indicating that the post-processing had changed the interaction of the polypeptide chains. In addition, the peak at 1255 cm^{-1} (amide III) was observed in the initial SF sample, owing to the random coil structure.[33] This result demonstrated that the random coils dominate the secondary structure of SF fibers collected by electrostatic spinning. However, the relevant peak did not appear in the treated samples, and a new peak at 1230 cm^{-1} was observed, which is related to the β-sheet structure.[34] In the C-C stretching vibration band, the peak of 1103 cm^{-1} corresponded to the α-helix structure that appeared in the initial SF sample, whereas the peak redshifted to 1082 cm^{-1} after post-processing, thereby indicating a change in the secondary structure of SF. Based on the above analysis, it can be concluded that ethanol solution will induce SF molecules to change their conformation, leading to an increase in the content of the β-sheet structure.

Meanwhile, the crystallinity ratio changes of the SF nanofiber membrane attributed to ethanol post-treatment were tested by X-ray Diffraction (Figure 2D). The spectra of initial SF exhibited two main diffraction peaks at $2\theta = 16.8°$ (α-helix) and 28.4° (β-turn), assigned to Silk I, and both the peaks shifted slightly to 17.3° and 28.7°, respectively, after treatment by ethanol and still the characteristic peaks of Silk I.[35] While the treated SF newly presented defined peaks at 2θ = 9.1° and 20.8° representative of β-sheet, which is associated with Silk II crystal.[36] The phenomenon suggests that the ethanol treatment of the samples resulted in the enrichment of crystalline structures. In addition, two other peaks are located at approximately 2θ = 38.7° and 42° in all spectra, which can be attributed to the superposition of other peaks.[36] The aforementioned results reveal that the ethanol strongly induced the Silk II (β-sheet) structure, improving the crystallinity. Because the crystallinity region of silk fibroin is made up of β-sheet, the degree of crystalline also reveals the content of β-sheet. Thus, the β-sheet structure in SF increased after treatment with ethanol.

Based on the above results, it can be concluded that the ethanol treatment has effectively changed the secondary structure of the silk fibroin. The process of the conformational transition is that the ethanol molecules penetrate the SF nanofiber and form a new hydrogen bond with the peptide chain of silk fibroin, thus dissociating the original intermolecular and intramolecular hydrogen bonds of the SF peptide chain. Then, the removal of ethanol by drying results in the recombination of the hydrogen bonds, which leads to a decrease in the α-helix, β-turn, and random roil structure and an increase in β-sheet structure. Furthermore, with the increase of the β-sheet in the secondary structure of SF, the crystallinity of the SF nanofiber also increases. Therefore, the hydrophobicity of the treated SF nanofiber membrane is enhanced from a macro perspective.

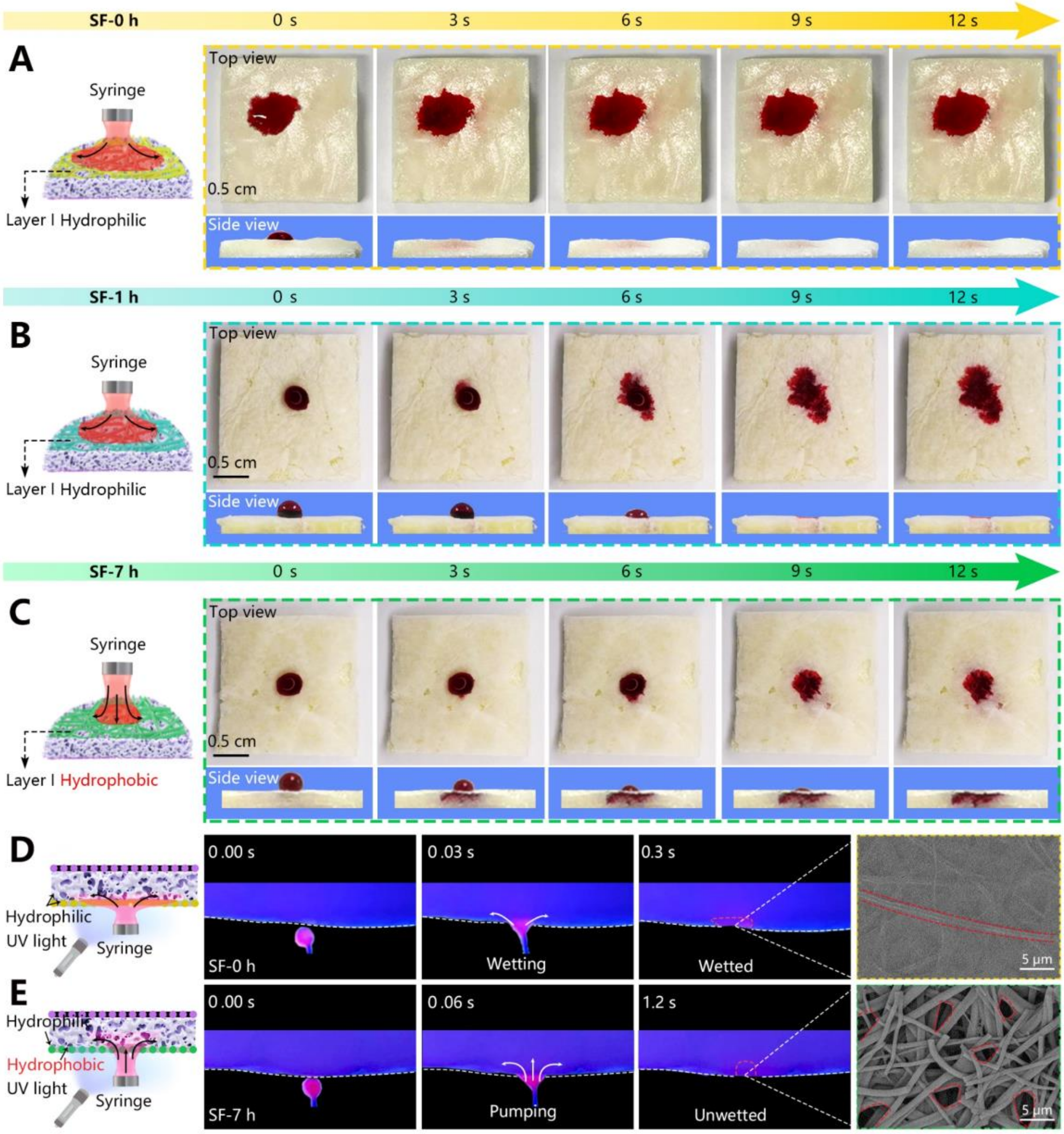

Figure 3. The diffusion and permeability of the red ink in the SSCG dressing with initial SF (A), treated with ethanol for 1h (B) and 7 h (C). Contact process between droplet (labeled with Rhodamine B) and SSCG dressing with initial SF (D) and treated SF (E) under UV radiation.

3.3. Water transport behavior in SSCG

To visually evaluate the wet permeability of SSCG, the water absorption test was designed by dripping a drop of red ink on the fiber membrane side. In Figure 3 A, it is clear to observe that red inks rapidly spread a small droplet point on the initial SF membrane. The absorbent sponge captured the droplet in three seconds, and the surface was wetted for a long time, which was not conducive to exudate export. Even though the ethanol post-process was used for 1 h when the red ink was added to the SF side of SSCG, the droplet was obviously diffused on the surface of the membrane first, and then part of the ink was absorbed by the sponge in the next layer through the SF membrane (Figure 3 B). A strong diffusion effect will lead to a weak osmotic effect, and the exudate left on the SF membrane will still make the wound overhydrated. Obviously, this phenomenon of inks spreading along the surface and slightly permeating through the dressing does not allow for the management of wound exudate. Thus, the treatment time of ethanol soaking was extended to 7 h. As can be seen from Figure 3 C, the diffusion effect of water was apparently weakened when dripping the same volume of red ink on the SF side, and almost all of the ink dripping on the SF side was absorbed by the sponge after infiltrating through the membrane.

To further demonstrate the antigravity water transportation behavior of the SSCG dressing, a simplified model was designed to simulate the management of wound exudate. In detail, the droplet labeled with Rhodamine B was squeezed out from a syringe and showed pink fluorescence under UV radiation. For the initial SF, the droplet rapidly wetted and was absorbed by the sponge layer, while the water was retained at the surface between the syringe and the initial SF (Figure 3 D). Moreover, the surface pore structure of the SF membrane disappeared once the droplet was absorbed. In comparison, the droplet was pumped through a treated SF membrane and temporarily stored in layer II (Figure 3 E). The layer I (post-treated SF) still maintained the porous structure, while the initial SF formed a complete membrane with embedded fibers, which closed the water transportation channel. These results suggest that the composite dressing has the capability to drain the fluid unidirectionally.

It is worth mentioning that the motion of water is a typical result of three acts. One is that the diffusion of ink along the surface of the membrane is caused by the wettability of the membrane, and the extent of diffusion is related to the surface hydrophilic degree of the membrane.[37] So the better the membrane is hydrophilic, the more the ink spreads on its surface. The second is to pass droplets through the membrane from the mesh between the fibers.[38] Because of the capillary effect, the ink on the net hole will pass through the mesh and reach the other side. The droplets on the net hole form a curved liquid surface because the liquid has surface tension, and there exists a pressure difference between the sides of the bending liquid side. Such pressure differential P_s is related to the curvature radius R and surface tension coefficient α of the liquid: $P_s = \frac{2\alpha}{R}$

Therefore, the pressure difference on both sides of the bending surface is proportional to the surface tension coefficient α of the liquid, and the curvature radius R of the liquid is inversely proportional. For this reason, the smaller the diameter of the intermesh hole, the more the liquid can penetrate the nanowires. Third, gravity is the force of water to be transported down, and gravity is a constant that is associated with its own mass.[39]

Continuity in exudate management relies heavily on four key structural characteristics: an interconnected porous structure that enables efficient water transport, hydrophilicity, thermal insulation properties, and surface photothermal conversion capabilities.[40] Inspired by the water evaporation and transpiration phenomenon observed in plants, the CS-KGM sponge, with its honeycomb-like structure and superabsorbent properties, enables efficient water transport from layer I to layer III. This facilitates the replenishment of water lost through evaporation. Moreover, acting as a pump in the water conducting process, the superabsorbent CS-KGM sponge exerts a draining force, resulting in a significant reduction in hydrostatic pressure.

While several models have been proposed to elucidate the mechanism of fluid conduction, including imbalanced Young's force[4], hydrophobic force[41], and Laplace pressure[39], the contact-pumping mechanism model appears to be more suitable for understanding water transportation in the SSCG.[20] In the SSCG composite dressing, the fluid can contact the hydrophilic sponge through the multiple hydrophobic–hydrophilic contacting points and the wetting force from the hydrophilic sponge would drive the fluid wetting the porous network.

Based on the abovementioned theories, the water conducting process of SSCG can be summarized as follows: the spread of droplets on the membrane is critical in these acts of water movement, the hydrophobic SF membrane and the hydrophilic CA membrane were selected as the layer I (the layer close to the skin) and the layer III (the layer away from the skin) respectively. When the SF side of SSCG was applied to the surface of the wound, the exudate passed through the SF membrane and was absorbed by the sponge, while the SF membrane prevented the exudate from hydrating the wound again. Due to the hydrophilicity of the CA membrane, exudate in the sponge tends to be adsorbed by the CA membrane so that exudate quickly wets the CA membrane and spreads on the surface.

3.4. Photothermal performance of SSCG dressing

Under the irradiation of NIR light, GO can absorb the energy of NIR light into thermal energy, resulting in temperature increases. Based on this feature, GO particles were homogeneously loaded on the CA single side. The principle of continuous export of exudate lies in the composite dressing exposed to NIR irradiation after absorption of exudate. Then, the surface temperature increases, and exudate in the sponge layer is evaporated into the air. To determine the final load capacity of GO, thermal infrared images and temperature changes of the CA membrane with different amounts of GO upon NIR irradiation were monitored.

As illustrated in Figure 4A, the irradiated temperature contour of CA membranes maintained a stable value around 32 ^oC during the exposure process. On the contrary, the surface temperature of CA membranes loaded with GO showed a drastic increase in the 1 min irradiation and tended to be stable after reaching the maximum value. Figure 4B suggests that the maximum temperature of each group increased with the load capacity of GO as well. Among them, the sample SSCG-3 exhibited a quick temperature increase from 29.1 ^oC to 53.2 ^oC. The higher the temperature, the faster the evaporation of exudate. At such high temperatures, thermal insulation of the sample is a critical factor to ensure the safe usage of the dressing in exudate management and wound healing. Under the same irradiation conditions, layer I of SSCG-3 maintained a low temperature of 31 ºC, leading to a significant temperature difference of 22.2 ºC between layer I and layer III. This phenomenon suggested that the SSCG-3 provided superior thermal insulation against heat transmission from the top to the bottom of the substrate. As shown in Figures 4C and 4D, a positive correlation was found between evaporation rate and Go concentration. In detail, the evaporation rate of SSCG-3 under NIR irradiation is approximately 6 times compared to natural evaporation. These results indicated that the loading of GO accelerates the evaporation of bioliquids, which can enhance continuous exudate management. Based on the above results, the SSCG-3 was chosen as the final sample.

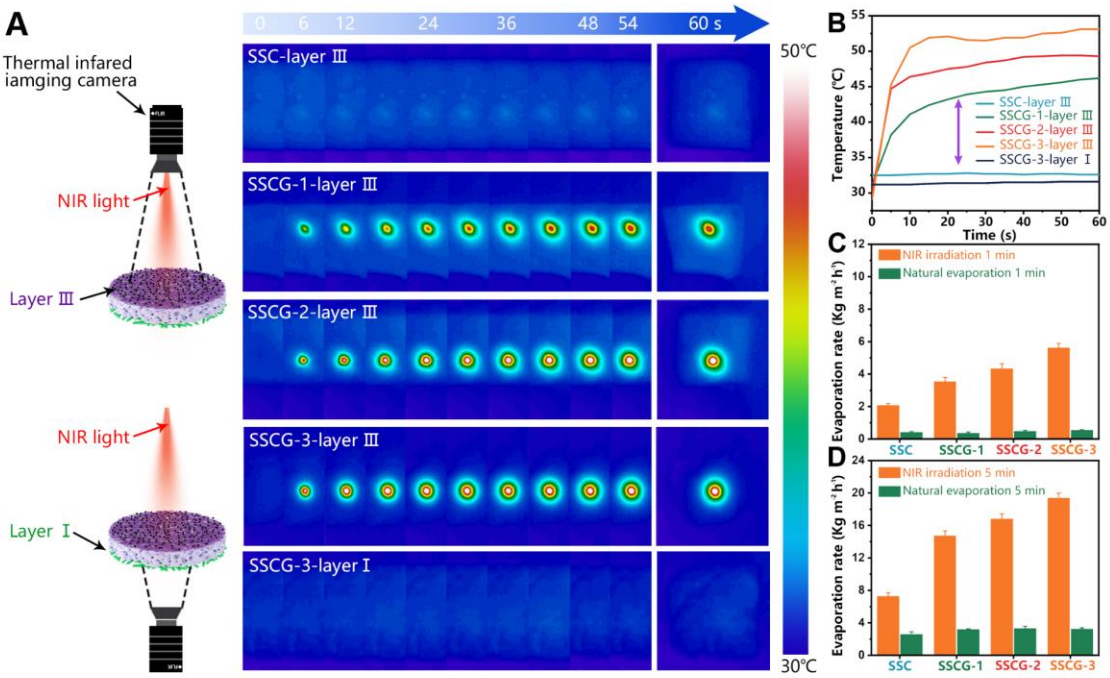

Figure 4. (A) Representative thermal infrared images and (B) temperature-time curves of layer I and layer III of samples. Evaporation rate of SSC, SSCG-1, SSCG-2, and SSCG-3 under NIR irradiation and natural conditions for 1 (C) and 5 min (D).

3.5. Assessment of the cell cytotoxicity

The cytotoxicity of the dressings was the primary evaluating indicator to appraise the effect of biomaterials on the growth of cells. Herein, the cytotoxicity of SSC, SSCG-1, SSCG-2, and SSCG-3 was tested. The live cells were stained green, and the dead cells with red in the fluorescent staining results. In Figure 5A, the SSC group without graphene oxide showed well-distributed L929 cells due to the excellent biocompatibility of raw material components. Despite the groups loaded with graphene oxide showing a slightly poorer distribution of cells, their proliferation is still better than that of the blank control. The MTT results were consistent with the staining assay (Figure 5B). In the SSCG-3 treated group, the cell viability was 101%. In addition, the side loaded with graphene oxide away from the wound should be noted. The aforementioned experimental findings provide evidence to support the non-cytotoxicity of the SSCG-3 dressing incorporated with graphene oxide.

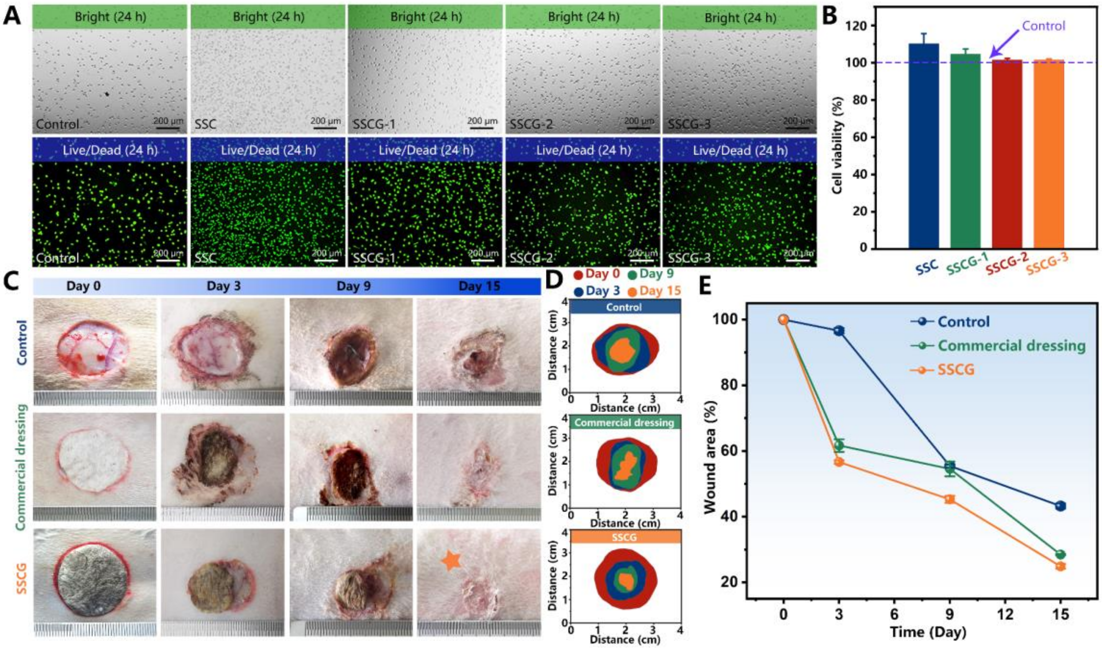

Figure 5. (A) Representative fluorescence staining images of live (green) and dead (red)

L929 cells treated with samples for 24 h. (B) MTT assay results. (C) Assessment of wound healing progress at various time intervals (0, 3, 9, and 15 days) for the control group, commercial dressing group, and SSCG. The graph depicts the change in wound size for each group over time. (D) Percentage wound photographs. (E) Statistical analysis of the relative trauma area.

3.6. Acceleration of wound healing by SSCG

To evaluate the reliability of SSCG dressing in wound management *in vivo*, full-thickness skin defect models of rabbits were created. Images of wound appearance after treatment for 3, 9, and 15 days were presented in Figure 5C. It is evident that as processing time increased, the relative wound area decreased in all three groups. In more detail, on the 3rd day, the relative wound area of the SSCG-treated group contracted to 56.6%, while it remained at 61.6% and 96.9% in the commercial-treated and blank control groups, respectively (Figure 5E). Similarly, whether 9 or 11 days after operations, the SSCG group consistently demonstrated significant advantages over the other groups. In addition, during the final healing stage, the wound site treated with the commercial product still exhibited a clearly visible scab, whereas the wound area had almost fully healed in the SSCG group. Based on the above results, it can be concluded that the application of SSCG effectively expedited the healing process, which could be attributed to the appropriate microenvironment management of SSCG dressing.

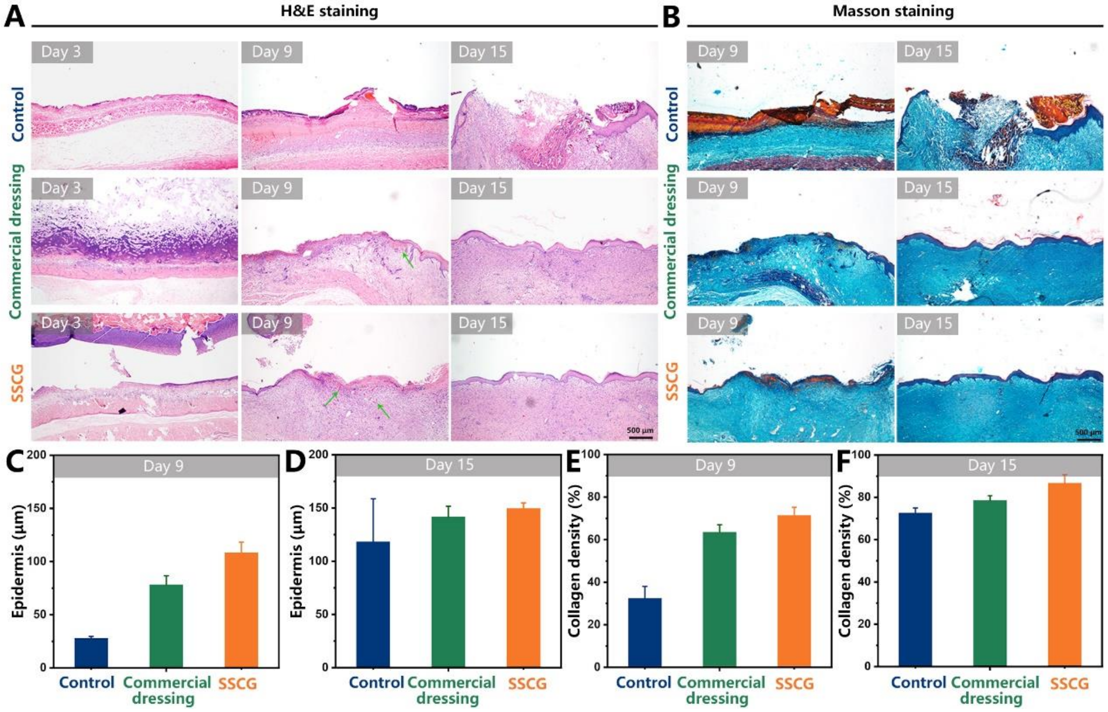

Figure 6. Micrographs of (A) H&E and (B) Masson Trichrome stained tissues during the healing process. (C-D) The measurement of epidermal thickness in skin tissue of each group at days 9 and 15. (E-F) Analysis of collagen density in Masson-stained tissue.

H&E and Masson Trichrome staining were performed to further assess the quality of initial re-epithelialization and collagen deposition. Figure 6A demonstrated a mild infiltration of inflammatory cells in both the commercial and SSCG groups during the initial stage of healing (day 3), which plays a favorable role in expediting the wound healing process. Moreover, although both the commercial and SSCG-treated groups completed the healing process beneath the scab on the ninth day, a higher presence of granulation tissues (as pointed out by the green arrows) was observed in SSCG groups that benefited wound repair. On day 15, the mature granulation tissue underwent a gradual replacement with collagen. In contrast to the fragmented epithelial structure observed in the blank control groups, the other treated groups exhibited complete repair with no presence of scabs. Notably, the group treated with SSCG demonstrated a more orderly re-epithelialization process and a uniform thickness in the epithelial layer. As shown in Figure 6B, a clear structure and tightly regenerated collagen fibers were observed in the SSCG-treated group. This phenomenon demonstrated that the SSCG group presented unparalleled wound repairing ability, which was attributed to the efficient wet permeability and the ideal bionic environment provided by the electrospun membrane. In addition, the assessment of new epidermis thickness and collagen density is crucial for wound healing and its healing quality. On days 9 and 15, the SSCG-treated group had the thickest central epidermis of the wound compared with the control and commercial groups (Figure 6C-D). In Masson staining, collagen is stained blue, and the intensity of the blue color is indicative of collagen density. The SSCG-treated group still shows the increased density of collagen deposition, albeit without statistical significance between the control and experimental groups (Figure 6F).

Conclusions

In summary, our study demonstrates that the composite dressing design effectively utilizes the porous structure of the sponge and electrospun membrane to facilitate the upward transportation of exudate. This transport mechanism is controlled by manipulating the proportion of secondary structure in silk fibroin, which directly impacts its hydrophilic properties. The spectral analysis demonstrated a marked alteration in the ratio of its secondary structure after soaking in ethanol. Our experiment has successfully confirmed the controllable transporting ability of the composite dressing. Additionally, the SSCG composite dressing can considerably improve wound closure, re-epithelialization, and collagen production during the healing process. This suggests that the dressing holds great promise for clinical development as an efficacious wound healing therapy.

Conflicts of interest:

The authors declare no conflicts of interest.

Acknowledgements

This work was supported by the Natural Science Foundation of Chongqing, China (cstc2020jcyj-msxmX0024 and cstb2022nscq-msx0555), the National Natural Science Foundation of China (No. 52103096), and the Fundamental Research Funds for Central Universities (Nos. SWU-XDPY22010).

References:

[1] Q. Zeng, X. Qi, G. Shi, M. Zhang, H. Haick, Wound Dressing: From Nanomaterials to Diagnostic Dressings and Healing Evaluations, ACS Nano 16(2) (2022) 1708-1733. https://doi.org/10.1021/acsnano.1c08411.

[2] Y. Dong, Y. Zheng, K. Zhang, Y. Yao, L. Wang, X. Li, J. Yu, B. Ding, Electrospun Nanofibrous Materials for Wound Healing, Adv. Fiber Mater. 2(4) (2020) 212-227. https://doi.org/10.1007/s42765-020-00034-y.

[3] F. Bao, G. Pei, Z. Wu, H. Zhuang, Z. Zhang, Z. Huan, C. Wu, J. Chang, Bioactive Self-Pumping Composite Wound Dressings with Micropore Array Modified Janus Membrane for Enhanced Diabetic Wound Healing, Adv. Funct. Mater. 30(49) (2020) 2005422. https://doi.org/10.1002/adfm.202005422.

[4] L. Liu, H. Sun, J. Zhang, B. Xu, Y. Gao, D. Qi, Z. Mao, J. Wu, Trilayered Fibrous Dressing with Wettability Gradient for Spontaneous and Directional Transport of Massive Exudate and Wound Healing Promotion, Adv. Fiber Mater. 5(2) (2023) 574-587. https://doi.org/10.1007/s42765-022-00239-3.

[5] S. Li, A. Chen, Y. Chen, Y. Yang, Q. Zhang, S. Luo, M. Ye, Y. Zhou, Y. An, W. Huang, T. Xuan, Y. Pan, X. Xuan, H. He, J. Wu, Lotus leaf inspired antiadhesive and antibacterial gauze for enhanced infected dermal wound regeneration, Chem. Eng. J. 402 (2020) 126202. https://doi.org/10.1016/j.cej.2020.126202.

[6] E. Guamba, N.S. Vispo, D.C. Whitehead, A.K. Singh, R. Santos-Oliveira, D. Niebieskikwiat, C. Zamora-Ledezma, F. Alexis, Cellulose-Based Hydrogels Towards an Antibacterial Wound Dressing, Biomater Sci 11(10) (2023) 3461-3468. https://doi.org/10.1039/D2BM01369J.

[7] M. Mirhaj, M. Tavakoli, J. Varshosaz, S. Labbaf, S. Salehi, A. Talebi, N. Kazemi, V. Haghighi, M. Alizadeh, Preparation of a biomimetic bi-layer chitosan wound dressing composed of A-PRF/sponge layer and L-arginine/nanofiber, Carbohydr. Polym. 292 (2022) 119648. https://doi.org/10.1016/j.carbpol.2022.119648.

[8] H. Zhang, C. Chen, H. Zhang, G. Chen, Y. Wang, Y. Zhao, Janus medical sponge dressings with anisotropic wettability for wound healing, Appl. Mater. Today 23 (2021)

101068. https://doi.org/10.1016/j.apmt.2021.101068.

[9] L. Zhou, P. Xu, P. Dong, X. Ou, X. Du, Y. Chen, X. Zhang, W. Guo, G. Gao, A self-pumping dressing with in situ modification of non-woven fabric for promoting diabetic wound healing, Chem. Eng. J. 457 (2023) 141108. https://doi.org/10.1016/j.cej.2022.141108.

[10] X. Zhang, R. Lv, L. Chen, R. Sun, Y. Zhang, R. Sheng, T. Du, Y. Li, Y. Qi, A Multifunctional Janus Electrospun Nanofiber Dressing with Biofluid Draining, Monitoring, and Antibacterial Properties for Wound Healing, ACS Appl. Mater. Interfaces 14(11) (2022) 12984-13000. https://doi.org/10.1021/acsami.1c22629.

[11] W. Yan, D. Miao, A.A. Babar, J. Zhao, Y. Jia, B. Ding, X. Wang, Multi-scaled interconnected inter- and intra-fiber porous janus membranes for enhanced directional moisture transport, J. Colloid Interface Sci. 565 (2020) 426-435. https://doi.org/10.1016/j.jcis.2020.01.063.

[12] A. Ahmed Babar, X. Zhao, X. Wang, J. Yu, B. Ding, One-step fabrication of multi-scaled, inter-connected hierarchical fibrous membranes for directional moisture transport, J. Colloid Interface Sci. 577 (2020) 207-216. https://doi.org/10.1016/j.jcis.2020.05.062.

[13] S. Shi, Y. Si, Y. Han, T. Wu, M.I. Iqbal, B. Fei, R.K.Y. Li, J. Hu, J. Qu, Recent Progress in Protective Membranes Fabricated via Electrospinning: Advanced Materials, Biomimetic Structures, and Functional Applications, Adv. Mater. 34(17) (2022) 2107938. https://doi.org/10.1002/adma.202107938.

[14] X. Wang, Z. Huang, D. Miao, J. Zhao, J. Yu, B. Ding, Biomimetic Fibrous Murray

Membranes with Ultrafast Water Transport and Evaporation for Smart Moisture-Wicking Fabrics, ACS Nano 13(2) (2019) 1060-1070. https://doi.org/10.1021/acsnano.8b08242.

[15] Z. Luo, L. Jiang, C. Xu, D. Kai, X. Fan, M. You, C.M. Hui, C. Wu, Y.-L. Wu, Z. Li, Engineered Janus amphipathic polymeric fiber films with unidirectional drainage and anti-adhesion abilities to accelerate wound healing, Chem. Eng. J. 421 (2021) 127725. https://doi.org/10.1016/j.cej.2020.127725.

[16] G. Huang, Y. Liang, J. Wang, X. Zeng, Z. Li, X. Zhang, Effect of asymmetric wettability on directional transport of water through Janus fabrics prepared by an electrospinning technique, Mater. Lett. 246 (2019) 76-79. https://doi.org/10.1016/j.matlet.2019.03.011.

[17] Y. Wang, G. Xia, H. Yu, B. Qian, Y.H. Cheung, L.H. Wong, J.H. Xin, Mussel-Inspired Design of a Self-Adhesive Agent for Durable Moisture Management and Bacterial Inhibition on PET Fabric, Adv. Mater. 33(35) (2021) 2100140. https://doi.org/10.1002/adma.202100140.

[18] Z. Zhang, W. Li, Y. Liu, Z. Yang, L. Ma, H. Zhuang, E. Wang, C. Wu, Z. Huan, F. Guo, J. Chang, Design of a biofluid-absorbing bioactive sandwich-structured Zn–Si bioceramic composite wound dressing for hair follicle regeneration and skin burn wound healing, Bioact. Mater. 6(7) (2021) 1910-1920. https://doi.org/10.1016/j.bioactmat.2020.12.006.

[19] Y. Lin, C. Wang, D. Miao, N. Cheng, N. Meng, A.A. Babar, X. Wang, B. Ding, J. Yu, A Trilayered Composite Fabric with Directional Water Transport and Resistance to

Blood Penetration for Medical Protective Clothing, ACS Appl. Mater. Interfaces 14(16) (2022) 18944-18953. https://doi.org/10.1021/acsami.2c03136.

[20] L. Shi, X. Liu, W. Wang, L. Jiang, S. Wang, A Self-Pumping Dressing for Draining Excessive Biofluid around Wounds, Adv. Mater. 31(5) (2019) 1804187. https://doi.org/10.1002/adma.201804187.

[21] R. Hu, N. Wang, L. Hou, J. Liu, Z. Cui, C. Zhang, Y. Zhao, Bilayer Nanoporous Polyethylene Membrane with Anisotropic Wettability for Rapid Water Transportation/Evaporation and Radiative Cooling, ACS Appl. Mater. Interfaces 14(7) (2022) 9833-9843. https://doi.org/10.1021/acsami.1c22974.

[22] C. Petit, J. Bachmann, L. Michalek, Y. Catel, E. Blasco, J.P. Blinco, A.-N. Unterreiner, C. Barner-Kowollik, UV-induced photolysis of polyurethanes, Chem. Commun. 57(23) (2021) 2911-2914. https://doi.org/10.1039/D1CC00124H.

[23] L. Xingtong, W. Zhentao, D. Tingting, G. Hongbo, G. Juan, Hydrogels from silk fibroin and multiarmed hydrolyzed elastin peptide, Surf. Innov. 8(4) (2020) 216-223. https://doi.org/10.1680/jsuin.19.00070.

[24] M. Sato, Y. Nakazawa, R. Takahashi, K. Tanaka, M. Sata, D. Aytemiz, T. Asakura, Small-diameter vascular grafts of Bombyx mori silk fibroin prepared by a combination of electrospinning and sponge coating, Mater. Lett. 64(16) (2010) 1786-1788. https://doi.org/10.1016/j.matlet.2010.05.024.

[25] Z. Shi, G. Lan, E. Hu, F. Lu, P. Qian, J. Liu, F. Dai, R. Xie, Puff pastry-like chitosan/konjac glucomannan matrix with thrombin-occupied microporous starch particles as a composite for hemostasis, Carbohydr. Polym. 232 (2020) 115814.

https://doi.org/10.1016/j.carbpol.2019.115814.

[26] Y. Li, X. Wang, Y.N. Fu, Y. Wei, L. Zhao, L. Tao, Self-Adapting Hydrogel to Improve the Therapeutic Effect in Wound-Healing, ACS Appl. Mater. Interfaces 10(31) (2018) 26046-26055. https://doi.org/10.1021/acsami.8b08874.

[27] Y. Wang, F. Lu, E. Hu, K. Yu, J. Li, R. Bao, F. Dai, G. Lan, R. Xie, Biogenetic Acellular Dermal Matrix Maintaining Rich Interconnected Microchannels for Accelerated Tissue Amendment, ACS Appl. Mater. Interfaces 13(14) (2021) 16048-16061. https://doi.org/10.1021/acsami.1c00420.

[28] G.M. Nogueira, A.C.D. Rodas, C.A.P. Leite, C. Giles, O.Z. Higa, B. Polakiewicz, M.M. Beppu, Preparation and characterization of ethanol-treated silk fibroin dense membranes for biomaterials application using waste silk fibers as raw material, Bioresour. Technol. 101(21) (2010) 8446-8451. https://doi.org/10.1016/j.biortech.2010.06.064.

[29] E. Casanova-Batlle, A.J. Guerra, J. Ciurana, Characterization of direct ink write pure silk fibroin based on alcohol post-treatments, Polym. Test. 116 (2022) 107784. https://doi.org/10.1016/j.polymertesting.2022.107784.

[30] X. Zhang, Z. Pan, Microstructure Transitions and Dry-Wet Spinnability of Silk Fibroin Protein from Waste Silk Quilt, Polymers 11(10) (2019) 1622. https://doi.org/10.3390/polym11101622.

[31] C. Yang, S. Shang, D. Shou, L. Ran, G. Lan, E. Hu, Transforming natural silk nonwovens into robust bioadhesives for in vivo tissue amendment, Journal of Cleaner Production 314 (2021) 127996. https://doi.org/10.1016/j.jclepro.2021.127996.

[32] Q.-N. Wei, A.-M. Huang, L. Ma, Z. Huang, X. Huang, P.-P. Qiang, Z.-P. Gong, L. Zhang, Structure regulation of silk fibroin films for controlled drug release, J. Appl. Polym. Sci. 125(S2) (2012) E477-E484. https://onlinelibrary.wiley.com/doi/abs/10.1002/app.36901.

[33] M. Zhao, Z. Qi, X. Tao, C. Newkirk, X. Hu, S. Lu, Chemical, Thermal, Time, and Enzymatic Stability of Silk Materials with Silk I Structure, Int. J. Mol. Sci. 22(8) (2021) 4136. https://doi.org/10.3390/ijms22084136.

[34] X.-G. Li, L.-Y. Wu, M.-R. Huang, H.-L. Shao, X.-C. Hu, Conformational transition and liquid crystalline state of regenerated silk fibroin in water, Biopolymers 89(6) (2008) 497-505. https://onlinelibrary.wiley.com/doi/abs/10.1002/bip.20905.

[35] R. Yadav, R. Purwar, Effect of post-treatment methods and nanoparticles on the conformation of silk fibroin and their impact on electrical properties, Polym-Plast. Tech. Mat. 61(18) (2022) 2016-2031. https://doi.org/10.1080/25740881.2022.2089576.

[36] M. Puerta, M.S. Peresin, A. Restrepo-Osorio, Effects of Chemical Post-treatments on Structural and Physicochemical Properties of Silk Fibroin Films Obtained From Silk Fibrous Waste, Front. Bioeng. Biotechnol. 8 (2020) 523949. https://doi.org/10.3389/fbioe.2020.523949.

[37] M. Cao, K. Li, Z. Dong, C. Yu, S. Yang, C. Song, K. Liu, L. Jiang, Superhydrophobic “Pump”: Continuous and Spontaneous Antigravity Water Delivery, Adv. Funct. Mater. 25(26) (2015) 4114-4119. https://doi.org/10.1002/adfm.201501320.

[38] Y. Si, C. Guo, X. Xu, K. Zhang, R. Tan, K.-t. Lau, J. Hu, Bioinspired Janus All-Natural Electrospinning Membranes with Directional Water Transport as Ecofriendly

Dry Facial Masks, ACS Sustain. Chem. Eng. 10(23) (2022) 7726-7738. https://doi.org/10.1021/acssuschemeng.2c02094.

[39] X. Tian, H. Jin, J. Sainio, R.H.A. Ras, O. Ikkala, Droplet and Fluid Gating by Biomimetic Janus Membranes, Adv. Funct. Mater. 24(38) (2014) 6023-6028. https://doi.org/10.1002/adfm.201400714.

[40] C. Jia, Y. Li, Z. Yang, G. Chen, Y. Yao, F. Jiang, Y. Kuang, G. Pastel, H. Xie, B. Yang, S. Das, L. Hu, Rich Mesostructures Derived from Natural Woods for Solar Steam Generation, Joule 1(3) (2017) 588-599. https://doi.org/10.1016/j.joule.2017.09.011.

[41] J. Wu, N. Wang, L. Wang, H. Dong, Y. Zhao, L. Jiang, Unidirectional water-penetration composite fibrous film via electrospinning, Soft Matter 8(22) (2012) 5996-5999. https://doi.org/10.1039/C2SM25514F.